Inhomogeneous distribution of lithium and electrolyte in aged Li-ion cylindrical cells

M.J. Mühlbauer[1-2], D. Petz[1, 3], V. Baran[1], O. Dolotko[1,4], M. Hofmann[1], R. Kostecki[5], A. Senyshyn[1,*]

[1]*Heinz Maier-Leibnitz Zentrum (MLZ), Technische Universität München, Lichtenbergstr. 1, 85748 Garching, Germany*

[2]*Institute for Applied Materials (IAM), Karlsruhe Institute of Technology (KIT), Hermann-von-Helmholtz-Platz 1, D-76344 Eggenstein-Leopoldshafen, Germany*

[3]*Lehrstuhl für Funktionelle Materialien, Physik-Department, Technische Universität München, James-Franck-Str. 1, 85748 Garching, Germany*

[4]*U.S. DOE Ames Laboratory, Iowa State University, Ames, Iowa 500011-3020, USA*

[5]*Energy Storage and Distributed Resources Division, Lawrence Berkeley National Laboratory, Berkeley, California 94720, USA*

Carbonate-based electrolytes in Li-ion batteries exhibit long range order in a frozen state, which enables their non-destructive analysis by diffraction methods. In the current study the spatial distribution of lithium and electrolyte inside the graphite anode was determined in cycled Li-ion cells using monochromatic spatially-resolved neutron diffraction measurements at 150 K. The results indicate a loss of lithium and electrolyte and their non-uniform distribution in the graphite anode in aged Li-ion cells. The observed lithium and electrolyte losses are directly correlated with two electrochemical performance degradation mechanisms, which are responsible for the cell capacity fade.

Keywords: *Li-ion batteries, 18650 – type, neutron diffraction, aging, electrolyte, lithium distribution*

Introduction

Excellent characteristics of Li-ion batteries, i.e. energy and power densities, cycle life, safety and no memory effect, made Li-ion technology dominant in the field of portable electronics and automotive applications. However, the industry constantly demands better performing Li-ion batteries at reduced cost. In fact, Li-ion battery

price $/kWh has been reduced by more than 80 % in the last decade. Among different components of Li-ion batteries the liquid electrolyte is an important factor defining battery safety, lifetime and long-term stability. The electrolyte potential stability window determines the application of the high-energy cathodes and anodes.Li-ion liquid electrolytes usually constitute of two or more organic carbonate solvents with different physical and chemical properties, which are mixed together in order to achieve the best electrochemical performance [1]. The majority of liquid electrolytes [2] used in commercial Li-ion cells is based on cyclic alkyl carbonates (ethylene carbonate EC) mixed with one or more linear carbonates (e.g. dimethyl carbonate (DMC), diethyl carbonate (DEC) or ethyl methyl carbonate (EMC)) and lithium salt (e.g. $LiPF_6$) with small amounts of additives [3] needed to fine tune the properties of the electrolyte mixtures.

The electrolyte in a Li-ion battery is partially consumed in electrochemical side-reactions on the anode [4, 5] or cathode [6, 7] surface and chemically decomposed at high temperature [8]. However, an accurate qualitative and quantitative monitoring of liquid electrolyte degradation processes (especially under *in operando* conditions) is a non – trivial experimental challenge due to electrolyte reactivity, flammability, corrosive properties, volatility as well as its sensitivity to temperature and high-energy spectroscopy and microscopy probes.. This technical difficulties may potentially be solved by diffraction techniques. In our recent work [9] we observed *in situ* local crystallisation of isolated LP30 electrolyte (Merck, 1 M $LiPF_6$ in EC/DMC 1/1 v/v) in $LiCoO_2$|C 18650 cells of using neutron diffraction at low temperatures.

Accurate quantification of electrolyte in Li-ion batteries by diffraction methods requires information about physical and chemical properties, crystal structure etc. Thermodynamic properties of Li-ion battery electrolytes were actively studied, whereas their crystal structure and thermal behaviour are well understood. In fact,

the crystal structure (C and O framework) of EC [10] and DEC [11] are reported in literature however, no structural information about DMC was published so far [12]. The majority of liquid electrolytes have relatively high freezing temperatures [13], which strongly depend on their chemical composition [14]. Furthermore, one may expect the crystal structure of an electrolyte to be more complex than its individual components [15].

The lithium ion conductivity of the liquid electrolyte drops by an order of magnitude when cooled from 25°C to -45°C [16]. One may expect its conductivity in frozen state even lower, which may further decrease/slow down the rate of battery charge-discharge process. This intrinsic behaviour of liquid electrolytes along with the lithium plating on the anode are believed to be the limiting factors for the usage of Li-ion batteries at low temperatures. *In situ* monitoring of electrolyte crystallization at low temperatures can help to quantify the amount of solid electrolyte in a lithium-ion battery and map its spatial distribution. The aim of the current work is to probe the amount and distribution of lithium in the negative electrode and the amount of frozen electrolyte in cylinder-type Li-ion batteries.

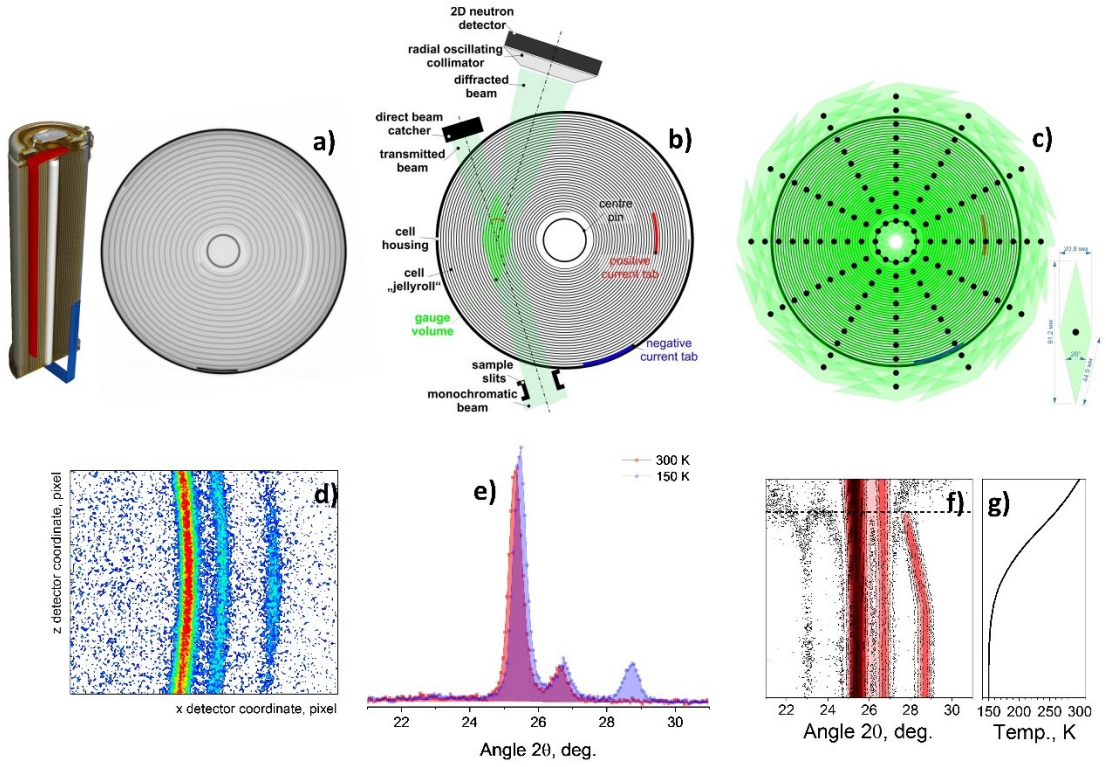

Fig. 1. ***Details of spatially-resolved experiments on studied NCA|C cells of 18650-type.*** *Typical layout of electrode and current tabs in the studied 18650-type cells as deduced by X-ray CT (a). Sketch of the gauge volume definition in spatially-resolved diffraction experiment (b) their in-plane configurations and shape of a single gauge volume (c). Typical 2D diffraction pattern obtained from a studied 18650 cell at 150 K (λ=1.615 Å), i.e. cross section of Debye – Scherrer cones with a flat 2D ^{3}He detector (d) and 1D diffraction data at T=150 K and T=300 K obtained by integration over detector height z (e) along with temperature evolution of 1D diffraction data upon cooling (f,g) – horizontal dashed line at T ≈260 K indicates an appearance of a long-range ordered signal resulting from the frozen electrolyte.*

Experimental

Battery cell:. The experimental studies were performed with commercial 18650-type 3,4 Ah Li-ion cells (NCR18650B, Panasonic) with a NCA – $LiNi_{0.80}Co_{0.15}Al_{0.05}O_2$ cathode and graphite anode. The cell layout and type is identical with "cell 3" reported in Ref. [17, 18], where double coated electrodes are wound around the centre pin (Fig. 1a). The anode is electrically connected by a current tab at the outer region of the cell, whereas the cathode is connected in the middle of its stripe.

Electrochemical testing: A batch of twenty pristine 18650-type cells was selected for electrochemical testing. The charge-discharge cycling was performed at room temperature using a Neware BTS 3000 potentiostat with a constant current (CC) constant voltage (CV) charge (U = 4.2 V, cutoff I=C/20), CC discharge (U = 2.5 V) protocol and 15 min rest at state-of-charge (SOC) SOC = 0 % and SOC = 100 %. The charging current was set to 1.675 A ≈ C/2 and to 6 A ≤ 2C for discharging. The cycling procedure was identical to our previous study [18] and the cells were cycled 60, 120, 210, 400, 600, 800, 1000, 1112 and 1392 times. A pair of cells was subjected to the same number of cycles. In order to achieve quasi-equillibrium cell conditions, prior the neutron diffraction experiment, all studied cells were “softly” charged and discharged CCCV/ CCCV (2.5-4.2 V, cutoff C/100, current 0.4 A ≈ 0.12 C) for three times using a VMP3 multichannel potentiostat (Bio-Logic, Inc.) with cycling process stopped at SOC = 100 %.

X-ray tomography: The internal cell layout (electrode and current tabs configuration) was studied using X-ray computed tomography, applying a v|tome|x s 240 tomography scanner (GE Phoenix). The applied X-Ray tube current and voltage were 100 µA and 130 kV, respectively. The data was collected in a cone beam geometry with a sensitive detector area of 200 mm x 200 mm corresponding to 1000 x 1000 image pixels. The adjustment of the magnification lead to an effective pixel size of 40 µm. A typical dataset contains 1000 projections, where each projection was obtained by the average of 3-4 single exposures of 1000 ms duration each. Data reduction and reconstruction was performed with the datos|x software from GE Phoenix. Final visualization of the data including the separation and colour coding of the cell constituents was performed using VGStudio MAX from VolumeGraphics. A characteristic slice of the obtained 3D image of a Li-ion cell is plotted in Fig. 1a.

Spatially-resolved neutron powder diffraction: The spatially-resolved neutron powder diffraction study was performed at the engineering diffractometer STRESS-SPEC at the neutron source FRM II (Garching b. München, Germany) [19]. A sketch of the experimental setup is displayed in Fig. 1b. The diffraction signal was obtained from a limited volume (gauge volume) defined by the collimation of the incident and scattered neutron beam at the given scattering angle. The incident monochromatic neutron beam (25‘ horizontal beam divergence, λ=1.615 Å) was shaped to 2 mm width and 17 mm height using the slit system in front of the sample. The scattered signal was analysed by a radial oscillating collimator with 2 mm horizontal field-of-view. A 2D position sensitive ^{3}He neutron detector (300 x 300 mm^2 active area, ca. 1000 mm sample-to-detector distance, central scattering angle 26 deg. 2θ) was used for data collection. The exposure time per single diffraction pattern was in the range of minutes. Different volumes of the studied sample were irradiated with accordance to the scheme shown in Fig. 1c.

The cycled Li-ion batteries at SOC=100 % (slowly CCCV charged using 0.4 A current) were mounted in a top-loading closed cycle refrigerator at ambient temperature, where Helium 4.6 was used as a heat transmitting gas. The temperature was controlled by a LakeShore 436 temperature controller and measured at a position close to the cell. The cooling time to lower the cell temperature to 150 K was ca. 2 hours. During cooling data collection was performed for a selected gauge volume of the fresh cell (Fig. 1 f,g).

A typical 2D diffraction dataset of the 18650 cell at 150 K (Fig. 1c) shows sections of Debye-Scherrer rings for three reflections. The homogeneous character of the intensity distribution along the diffraction rings in vertical direction indicates no contribution from sharp preferred orientation in diffraction intensities. The 2D diffraction data were corrected for detector nonlinearities, geometrical aberrations,

curvature of diffraction rings and finally integrated over detector height using the program package STECA [20].

High-resolution neutron powder diffraction: The high-resolution neutron powder diffraction studies were performed at SPODI at FRM II [21]. Data collection was carried out in Debye-Scherrer geometry with an incident neutron beam having a rectangular cross section of 40×20 mm^2. Monochromatic neutrons with a wavelength of 1.54832(4) Å were obtained from the (551) reflection of a vertically focused composite germanium monochromator at 155° take-off angle. 2D diffraction data were collected in the range of 4-152° 2θ and corrected for geometrical aberrations using the algorithm reported in Ref. [22].

Analysis of diffraction data: The main emphasis was made on the analysis of structural evolution of $00l$ reflections from a mixture of stage I (LiC_6) and II (LiC_{12}) of graphite lithium intercalation compound [17]. The well defined structure of LiC_6 and LiC_{12} compounds, which exist in a very narrow homogeneity range causes the change of lithium concentration in the charged graphite anode to be reflected in the fraction of stage I and stage II. The LiC_6/LiC_{12} ratio has been proven to be very sensitive to the graphite anode state-of-charge [23], degree of electrode degradation [24] and cell temperature [25]. The couple of (001) LiC_6 (25.5° 2Θ) and (002) LiC_{12} (26.5° 2Θ) reflections (in first approximation corresponding to the interplanar distances between the graphite sheets in these compounds) is well suited for the quantification of relative phase fractions of stage I and II due to their high-intensity and non-overlapping character – high angular splitting. The third peak present at Figs. 1d,e,g (ca. 28.8° 2θ) was attributed to the (002) reflection from the frozen electrolyte.

Molar quantities of LiC_6 vs. LiC_{12} were determined from the diffraction data as $N=I_{hkl}[V/F_{hkl}]^2[M/\rho]$, where I_{hkl} is the observed intensity of the Bragg reflection with

Miller indices hkl, F_{hkl} is the corresponding structure factor, V is the cell volume, M and ρ are the molar weight and density of the phase under consideration. Using the structure factors F_{001}= 4.197 (LiC_6) and F_{002}= 8.022 (LiC_{12}) along with the cell volumes V_{LiC6}= 59.676(8) Å^3 and V_{LiC12}= 112.284(9) Å^3 the LiC_6 to LiC_{12} molar ratio (n_{LiC6}:n_{LiC12}) can be determined. For the sake of clarity, it is more convenient to work with a single parameter $n_1[LiC_6] + n_2[LiC_{12}] \rightarrow n[LiC_6] + (1-n)[LiC_{12}] = z[Li_xC_6]$, i.e. to switch to a relative (mean) lithium concentration x in the lithiated graphite Li_xC_6 defined as $x=6/(12-6n_{LiC6}) = 1/(2-n_{LiC6})$ [17]. This will yield x=1 in Li_xC_6 for a pure stage I with n_{LiC6}=1.0, whilst for stage II it will become x=0.5. Extending the same treatment to the electrolyte by using its structure factor F_{002}= 10.445 (electrolyte) and cell volume $V_{electr.}$=450.6 Å^3 the phase relationship is modified as follows $n_1[LiC_6] + n_2[LiC_{12}] + n_3[\text{Electrolyte}] \rightarrow y[Li_xC_6] + n_3[\text{Electrolyte}] \rightarrow [Li_xC_6] + m[\text{Electrolyte}]$, where coefficient $m=\frac{n_3}{2-n_{LiC_6}}$ defines the electrolyte concentration normalized to the molar amount of lithiated graphite.

Results and discussion

The 18650 Li-ion cells exhibited gradual loss of capacity during cycling (Fig. 2a). Initial discharge capacities of the cells were approx. 3.17 Ah – notably smaller than the nominal capacity of 3.4 Ah, which is attributed to the relatively high charge/discharge currents.

As mentioned in Ref. [18], at the given cycling conditions a reduced discharge capacity of 80 % is reached after approx. 110 cycles already and after 400 cycles only 60 % of initial capacity can be retained. Besides this a certain spread in state-of-health vs. cycle number (horizontal dotted line in Fig. 2a at ca. 1.25 Ah capacity) has been found reaching up to ±15%, which is associated with the accelerated cell aging close to the limits of the specifications. Below 550±100 cycles the decay of cell capacity can be approximated by the square root of time dependence

corresponding to diffusion-limited SEI growth [26], which might be further supplemented by the loss of movable lithium [24]. Above ca. 600 cycles under the given cycling conditions the cell capacity rapidly fades and above 850 cycles the cell capacity falls down to nearly zero.

The rapid loss of cell performance in the region between 600 and 810 cycles is supplemented by changes of the voltage profile during charge-discharge cycle (Fig. 2c). After an initial voltage drop due to resistance of the cell the voltage raises again, which can be associated with a self-heating due to Ohmic losses. The internal cell resistance was estimated at SOC = 0 % and SOC = 100 % of each cycle from the potential drop occurring when switching on and switching off the 6 A discharge current [27]. The obtained cell resistances have been found different in fully charged and fully discharged state, where both show an increase vs. cycle number (Fig. 2b). One may see that at ca. 810 -850 cycles the internal cell resistance at SOC = 0 % rapidly increases, which is responsible for the initial voltage drop from 4.2 to 2.5 V. Using pulse charge/discharge (400 mA current) the SOC dependence of internal resistance was determined for the whole series of studied cells and plotted in false colours for charge (Fig. 2d) and discharge (Fig. 2e) states.

Cyclic voltammetry data was collected for all studied cells, where upon cell charge one clearly resolves peaks at 3.4, 3.66, 3.92 V and 4.1V for fresh state. According to [28] the signal at 3.4 V is attributed to C-Li_xC_6 formation, whereas other peaks are often assigned to structural phase transformations in electrode materials occurring upon cell charge/discharge. A remarkable lithiation/delithiation voltage hysteresis $\Delta U \approx 0.1$ V can be noted, which can be primarily associated with the internal resistance of the wound electrode stack. Cell fatigue further increases observed voltage hysteresis by shifting characteristic peaks towards higher voltages upon cell charge and, accordingly, to lower potentials during discharge. Cell aging is manifested by broadening of the observed peaks, which can be understood by

merging of the corresponding voltage plateaus, caused by local SOC non-uniformities.

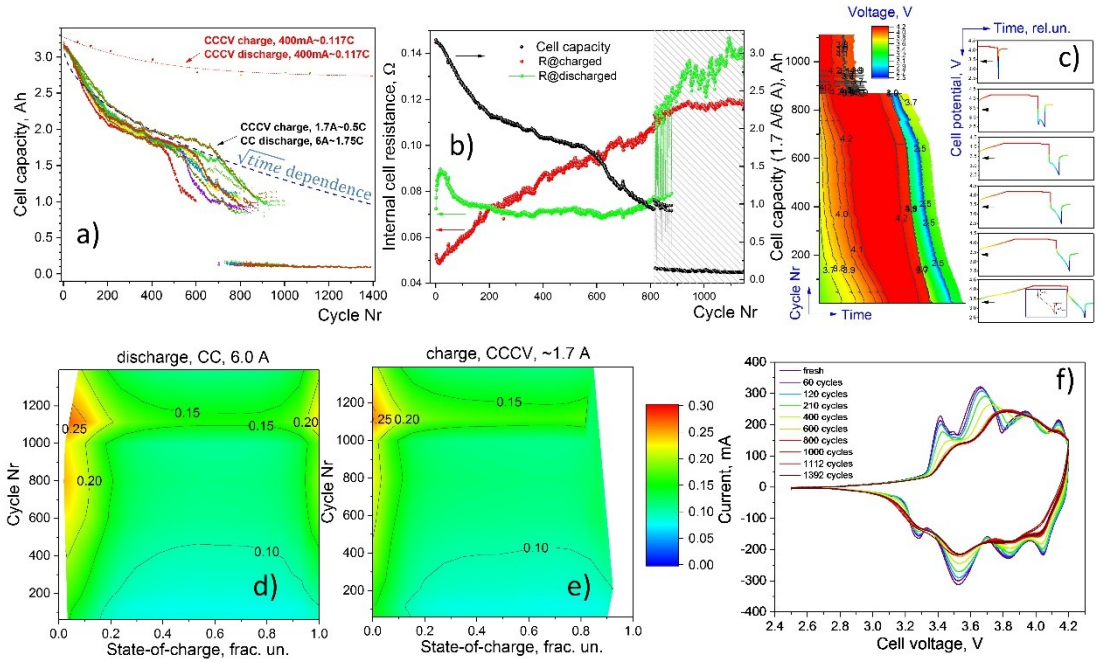

Fig. 2. ***Results of electrochemical characterisation.*** *Evolution of cell capacity vs. cycling (a), internal cell resistance (determined from the potential drop) at SOC=0 % and SOC=100% (b) and evolving of potential profile with the cycle number (c); color coded internal cell resistance vs SOC and cycle number obtained from pulsed discharge (d) and charge (e); changes in cyclic voltammogram for differently cycled cells (f).*

For this purpose, the cell local SOC variation was probed using spatially-resolved neutron diffraction, with characterisation of lithium concentration in the graphite anode at 5 different planes perpendicular to cylinder axis (Fig. 3). The cells were cycled at ambient temperature, but the collection of diffraction data was performed at 150 K. Low temperatures have been found affecting the state of the graphite anode in Li-ion batteries [29], even with no SOC changes applied. In Ref. [25] an anomalous thermal expansion in LiC_6 above 250 K was reported along with a decrease of the Debye temperature (lattice softening) of the Li_xCoO_2 cathode in delithiated state (SOC = 100 % of LIB). Low-lithiated graphites ($LiC_{y>12}$) have been found thermally unstable at low temperatures [9]. The main feature, however, is

the crystallisation of liquid electrolyte, similar to the observed $LiCoO_2$|C cylinder cell in Ref. [9]. It can be illustrated by the stack of diffraction data in Fig. 1f, where at room temperature the two well resolved (001) and (002) reflections of stage I (LiC_6) and stage II (LiC_{12}) lithiated graphites are present at 24.4° and 26.6° 2θ[1]. Cooling the cell to 150 K resulted in the appearance of an additional diffraction signal at ca. 28.8° 2θ at temperatures below 260 K, which was attributed to the (002) reflection of an ordered electrolyte structure.

The diffraction intensities of the (001)/(002) LiC_6/LiC_{12} reflection doublet enable for a determination of the lithiation state x in the anode Li_xC_6. The spatial lithium distribution in the middle plane of the studied cell type was already reported at ambient temperature [17], where a homogeneous lithium behaviour was observed. Taking into consideration the intensities of the frozen electrolyte permits its quantification as weight or molar fraction with respect to the lithiated graphites (see Analysis of collected diffraction data section).

The lithium concentration x in the lithiated graphite anode Li_xC_6 was studied for a fresh and a cell cycled 600 times (see plot in Fig. 3a). The aged cell displays sufficiently lower lithium concentrations, which can be attributed to the fatigue-driven losses of the movable lithium [24] along with non-uniformities of its distribution. For example, systematically lower lithium concentrations at the top and bottom of the aged cell were observed, which is in agreement with recent X-ray diffraction radiography studies on harvested anode stripes [18]. The observed changes in lithium distribution can be attributed to different factors, e.g. presence of pressure\temperature gradients, local gas formation, electrolyte wetting, current distribution etc.

[1] Instantaneous temperature profile is plotted in Fig. 1f.

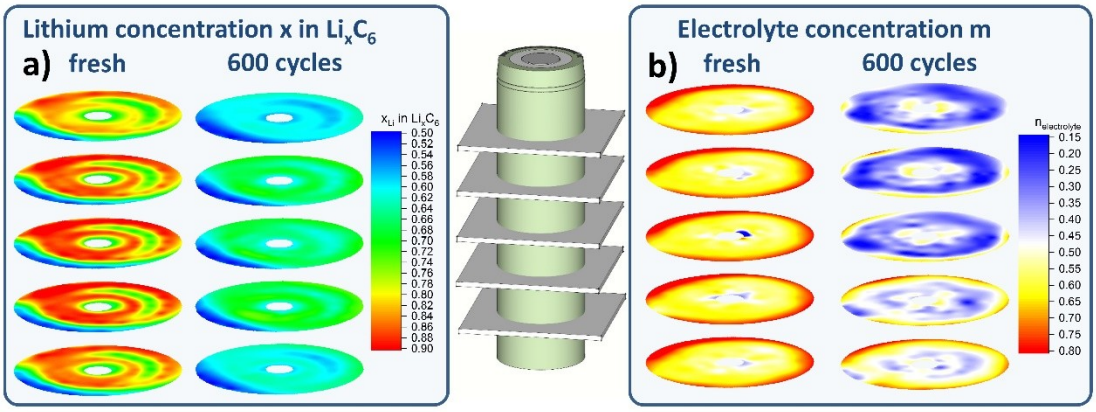

Fig. 3. ***Lithium and electrolyte concentrations*** *at different planes of fresh and aged (600 cycles) studied cylinder cells.*

Among these factors, the electrolyte dynamics is the less studied one. It is a complex task since it couples fluid dynamics and electrochemistry and will strongly depend on cell layout, chemistry, morphology *etc*. There were several attempts to tackle this problem using imaging methods [18, 30], which, however, have rather qualitative character. Therefore, the 2D distributions of the frozen electrolyte concentration in a fully charged fresh and an aged 18650-type cell were extracted from the obtained diffraction data and are presented in Fig. 3b. Within the studied plane a non-uniform 2D behaviour of the frozen electrolyte concentration is observed, which is reflected in noticeably higher concentrations at the outer cell region. This can be explained by the natural gap between the electrode materials and the cell housing, which is filled with the liquid electrolyte at SOC=100% and plays the role of electrolyte reservoir. In contrast to radial non-uniformities, the in-plane pictures collected at different heights of the fresh cell have been found very similar showing that the electrolyte is quasi-uniformly distributed over the cell height. Introduced cell aging seriously changes the situation: similar to the lithium behaviour a sufficient reduction of the electrolyte concentration is observed; electrolyte is placed in higher residues close to the cell surface; a serious

concentration gradient from cell top to bottom appears with the majority of the electrolyte located at the cell bottom[2].

Differences in the patterns of non-uniform concentrations for lithium and electrolyte are very important, showing complex degradation mechanism of the cell components during cycling. Localisation of the electrolyte excess at the bottom of 18650-type cell can be equally associated with both gravity effects and with the periodic volumetric expansion/shrinking of the electrodes upon cell cycling, and corresponding electrolyte percolation in the composite electrode pores.

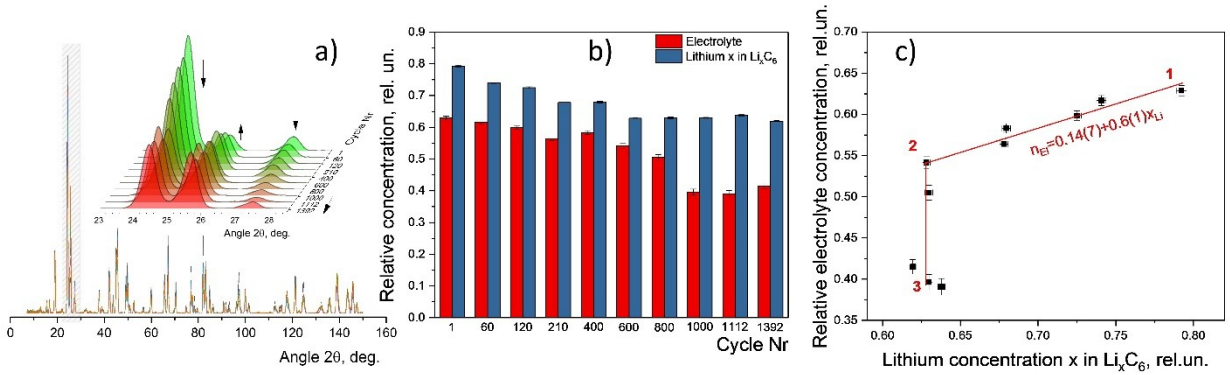

Fig. 4. High-resolution neutron diffraction data (a) obtained on differently cycled 18650 cells at 150 K (inset illustrates the intensity distribution in 001 : 002 : 002 for LiC_6 : LiC_{12} : electrolyte peak triplet vs. fatigue); dependence of lithium concentration in the graphite anode and electrolyte vs. cycle number (b); relationship between lithium and electrolyte concentrations in variously cycled cells (c).

To find the correlation between remaining lithium concentration in the anode and the amount of electrolyte, the set of previously mentioned aged cells was characterised using high-resolution neutron powder diffraction at 150 K. In contrast to spatially-resolved neutron diffraction, this experiment results in mean values for both the lithium and the electrolyte concentration (*quasi* volume averaged). Obtained diffraction data are plotted in Fig. 4a, where inset to Fig. 4a illustrates a systematic decrease of the intensity ratio of the (001)/(002) LiC_6/LiC_{12} reflection

[2] The cell was cycled, stored and measured in its standard vertical configuration, i.e. with safety vent at the top.

couple upon increasing cycle number, which is also supplemented by a reduction of the intensity for the observed 002 reflection of the frozen electrolyte. Extracted concentrations of lithium and electrolyte are plotted vs. cycle numbers in the form of bar graphs (Fig. 4b). Both concentrations display reducing tendencies with slightly different character. For sake of clarity the x in Li_xC_6 was plotted vs. the relative electrolyte concentration (Fig. 4c) and clearly shows two regimes of the lithium vs. electrolyte dependence. In the first regime (points 1-2) the loss of movable lithium is linearly proportional to the loss of electrolyte. At point 3 - corresponding to 600 cycles (a point where accelerated capacity fading starts) the behaviour is totally changed: no further loss in the lithium concentration in the anode is observed, whilst an obvious reduction of electrolyte takes place (line 2-3). These two regimes can be further correlated to the cycling behaviour of the studied cells (Fig. 2a). A linear correlation of lithium and electrolyte losses is attributed to the reduction of cell capacity. The “diffusion limited” character of capacity reduction directly relates it to the growth of SEI where heterogeneities build up. Both accelerated formation of SEI along with non-uniform cell composition give rise to higher overpotentials, which are believed to be the reason for the accelerated capacity fading and electrolyte decomposition in regime 2.

Conclusions

In summary, the effect of low-temperature induced crystallisation of liquid electrolyte and neutron diffraction were successfully applied for non-destructive mapping of electrolyte distribution in pristine and cycled 18650 commercial Li-ion cells. The cells were cycled using the maximum current rates allowed by the cell manufacturer and short rest times, which caused a rapid cell degradation. It is worth to mention that applying only a current of 1C discharge to the studied cell type (instead of 2C reported in the current study) results in no visible anomalies of

the cell capacity evolution below 3000 cycles, i.e. no accelerated capacity fading occurs.

The lithium amount in the lithiated graphite electrode Li_xC_6 and the electrolyte concentration were monitored using neutron diffraction, irradiating either the entire 18650 cell in a standard neutron diffraction experiment or small gauge volumes applying spatially-resolved neutron powder diffraction. Except those regions around current tabs and where the anode and cathode do not overlap [18], the lithium distribution in the fresh cell was found fairly uniform. The electrolyte in the fresh cell at SOC=100 % has been found predominatly localised in the outer part of the cell spiral wound, which can explain the systematically higher lithiation of the graphite anode typically observed in outer region of aged cells [31]. The distributions of both lithium and electrolyte in the fresh cell had been found uniform across the cell spiral wound height. Similar analysis of the cell cycled 600 times revealed a reduction of the lithium and electrolyte amounts, which is accompanied by an appearance of pronounced cell non-uniformities over the cell height with accumulation of electrolyte in the bottom section of the cylindrical cell.

Analysis of the relationship between the lithium and electrolyte average distribution in the cell produced the following observations:

(1) a clear linear correlation between loss of lithium in graphite and loss of electrolyte in the cell can be concluded at the initial stage of cell operation (when the cell capacity loss is proportional to $\sqrt{time}$);

(2) at higher degrees of cell fatigue an accelerated capacity fading is observed, which is characterised by a fast consumption of electrolyte and no change in the average lithium concentration.

The linear correlation of lithium and electrolyte losses during the “normal” cell fatigue unambiguously shows that during the fatigue process the free movable

lithium is trapped by electrolyte decomposition products (e.g. SEI), which is the main mechanism of fatigue in the studied Li-ion cells. The proposed experimental approaches could be applied to a broad range of Li-ion cells based on graphite anode and potentially open up promising perspectives of testing different charging protocols, storage and calendaring processes as well as electrolyte additives with respect to their correlations of lithium and electrolyte losses.

Acknowledgement

The authors gratefully acknowledge the financial support provided by the Heinz Maier-Leibnitz Zentrum (Technische Universität München), German Federal Ministry of Education and Research (BMBF Projects 05K16VK2 and 05K19VK3) and Bavaria California Technology Center (BaCaTeC, project 14[2014-02]). This work was supported by the Assistant Secretary for Energy Efficiency and Renewable Energy, Vehicle Technologies Office, under the Advanced Battery Materials Research (BMR) Program, of the U.S. Department of Energy under Contract No. DE-AC02-05CH11231f. Authors thank the Heinz Maier-Leibnitz Zentrum for the access to their research infrastructure.

References

[1] J.M. Tarascon, D. Guyomard, Solid State Ionics, 69 (1994) 293-305.
[2] K. Xu, Chemical Reviews, 114 (2014) 11503-11618.
[3] A.M. Haregewoin, A.S. Wotango, B.-J. Hwang, Energy & Environmental Science, 9 (2016) 1955-1988.
[4] H.H. Lee, C.C. Wan, Y.Y. Wang J Electrochem Soc, 151 (2004) A542-A547.
[5] M. Herstedt, D.P. Abraham, J.B. Kerr, K. Edström, Electrochimica Acta, 49 (2004) 5097-5110.
[6] D.P. Abraham, R.D. Twesten, M. Balasubramanian, J. Kropf, D. Fischer, J. McBreen, I. Petrov, K. Amine, J Electrochem Soc, 150 (2003) A1450-A1456.
[7] D. Aurbach, K. Gamolsky, B. Markovsky, G. Salitra, Y. Gofer, U. Heider, R. Oesten, M. Schmidt, J Electrochem Soc, 147 (2000) 1322-1331.
[8] C.L. Campion, W. Li, B.L. Lucht, J Electrochem Soc, 152 (2005) A2327-A2334.

[9] A. Senyshyn, M.J. Muhlbauer, O. Dolotko, H. Ehrenberg, Journal of Power Sources, 282 (2015) 235-240.
[10] C. Brown, Acta Crystallographica, 7 (1954) 92-96.
[11] A.A. Yakovenko, J.H. Gallegos, M.Y. Antipin, A. Masunov, T.V. Timofeeva, Crystal Growth & Design, 11 (2011) 3964-3978.
[12] P. Whitfield, I.J. Davidson, Meeting Abstracts, MA2010-03 (2010) 163.
[13] D. Yaakov, Y. Gofer, D. Aurbach, I.C. Halalay, J Electrochem Soc, 157 (2010) A1383-A1391.
[14] M.S. Ding, K. Xu, S. Zhang, T.R. Jow, J Electrochem Soc, 148 (2001) A299-A304.
[15] A. Abouimrane, P.S. Whitfield, S. Niketic, I.J. Davidson, Journal of Power Sources, 174 (2007) 883-888.
[16] T. Okumura, T. Horiba, Journal of Power Sources, 301 (2016) 138-142.
[17] A. Senyshyn, M.J. Muhlbauer, O. Dolotko, M. Hofmann, H. Ehrenberg, Sci Rep, 5 (2015) 18380.
[18] D. Petz, M.J. Mühlbauer, V. Baran, M. Frost, A. Schökel, C. Paulmann, Y. Chen, D. Garcés, A. Senyshyn, Journal of Power Sources, 448 (2020) 227466.
[19] M. Hofmann, R. Schneider, G.A. Seidl, J. Rebelo-Kornmeier, R.C. Wimpory, U. Garbe, H.G. Brokmeier, Physica B: Condensed Matter, 385-386 (2006) 1035-1037.
[20] C. Randau, U. Garbe, H.-G. Brokmeier, J Appl Crystallogr, 44 (2011) 641-646.
[21] M. Hoelzel, A. Senyshyn, O. Dolotko, Journal of large-scale research facilities JLSRF, 1 (2015) A5.
[22] M. Hoelzel, A. Senyshyn, N. Juenke, H. Boysen, W. Schmahl, H. Fuess, Nuclear Instruments and Methods in Physics Research Section A: Accelerators, Spectrometers, Detectors and Associated Equipment, 667 (2012) 32-37.
[23] A. Senyshyn, O. Dolotko, M.J. Muhlbauer, K. Nikolowski, H. Fuess, H. Ehrenberg, J Electrochem Soc, 160 (2013) A3198-A3205.
[24] O. Dolotko, A. Senyshyn, M.J. Muhlbauer, K. Nikolowski, F. Scheiba, H. Ehrenberg, J Electrochem Soc, 159 (2012) A2082-A2088.
[25] V. Baran, O. Dolotko, M.J. Mühlbauer, A. Senyshyn, H. Ehrenberg, J Electrochem Soc, 165 (2018) A1975-A1982.
[26] H.J. Ploehn, P. Ramadass, R.E. White, J Electrochem Soc, 151 (2004) A456-A462.
[27] H.-G. Schweiger, O. Obeidi, O. Komesker, A. Raschke, M. Schiemann, C. Zehner, M. Gehnen, M. Keller, P. Birke, Sensors (Basel), 10 (2010) 5604-5625.
[28] R. Jung, M. Metzger, F. Maglia, C. Stinner, H.A. Gasteiger, J Electrochem Soc, 164 (2017) A1361-A1377.

[29] C.K. Huang, J.S. Sakamoto, J. Wolfenstine, S. Surampudi, J Electrochem Soc, 147 (2000) 2893-2896.
[30] M. Lanz, E. Lehmann, R. Imhof, I. Exnar, P. Novák, Journal of Power Sources, 101 (2001) 177-181.
[31] M.J. Muhlbauer, O. Dolotko, M. Hofmann, H. Ehrenberg, A. Senyshyn, Journal of Power Sources, 348 (2017) 145-149.